RISensing: Leveraging Reconfigurable Intelligent Surfaces to Empower Wi-Fi Sensing

Xiaojing Wang, Binbin Xie, Guanghui Lv, Boyang Liu, Chenhao Ma, Renjie Zhao, Chao Feng, Xiaojiang Chen

Abstract—Wi-Fi technology has emerged as a promising solution for contact-free sensing owing to the pervasiveness of Wi-Fi signals in indoor environments. However, Wi-Fi sensing faces several fundamental issues, including limited sensing range and unstable orientation-dependent sensing performance, hindering the widespread adoption of Wi-Fi sensing in real-life scenarios. In this paper, we propose RISensing, a novel system that leverages Reconfigurable Intelligent Surfaces (RIS) to address these two fundamental issues of Wi-Fi sensing and bring Wi-Fi sensing one step closer to real-world adoption. Unlike prior Wi-Fi sensing works which typically rely on a single target reflection signal to capture the target movement, RISensing utilizes two target reflection signals, i.e., the direct target reflection signal and RIS-based target reflection signal, to boost the sensing capability. RISensing characterizes the RIS-based target reflection signal, and constructively combines it with the direct target reflection. We evaluate the sensing performance of RISensing in various environments, including corridor, office and lab. Extensive experiments demonstrate RISensing can improve the sensing range of Wi-Fi from 4 m to 23 m, and effectively mitigate the orientation-dependent issue.

Index Terms—Wi-Fi sensing, Reconfigurable intelligent surface (RIS), Sensing range

I. INTRODUCTION

In recent years, we have witnessed the rapid advancement of wireless sensing which is capable of capturing human motion

Xiaojing Wang is with the Shaanxi Key Laboratory of Passive Internet of Things and Neural Computing, School of Information Science and Technology, Northwest University, Xi'an 710127, China (e-mail: wxj@stumail.nwu.edu.cn).

Binbin Xie is with the Department of Computer Science and Engineering, University of Texas at Arlington, Arlington, TX 76019, USA (e-mail: binbin.xie@uta.edu).

Guanghui Lv is with the Shaanxi International Joint Research Centre for the Battery-Free Internet of Things, School of Information Science and Technology, Northwest University, Xi'an 710127, China (e-mail: luguanghui@stumail.nwu.edu.cn).

Boyang Liu and Chenhao Ma are with the Xi'an Key Laboratory of Advanced Computing and System Security, School of Information Science and Technology, Northwest University, Xi'an 710127, China (e-mail: liuboyang@nwu.edu.cn, machenhao@stumail.nwu.edu.cn).

Renjie Zhao is with the Department of Computer Science, Johns Hopkins University, Baltimore, MD 21218, USA (e-mail: rjzhao@jhu.edu).

Chao Feng is with the Xi'an Advanced Battery-Free Sensing and Computing Technology International Science and Technology Cooperation Base, School of Information Science and Technology, Northwest University, Xi'an 710127, China (e-mail: chaofeng@nwu.edu.cn).

Xiaojiang Chen is with the Internet of Things Research Center, School of Information Science and Technology, Northwest University, Xi'an 710127, China (e-mail: xjchen@nwu.edu.cn).
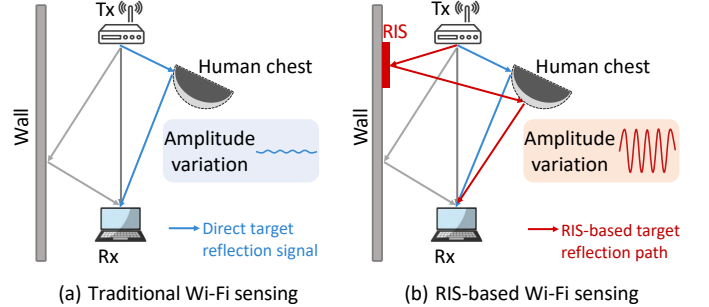

Figure 1: Prior Wi-Fi sensing vs RIS-based Wi-Fi sensing.

without requiring any devices to be attached to human body. The underlying principle of wireless sensing is that the signals can be reflected from human body, and by analyzing the signal variation induced by human motion, valuable information about the motion can be obtained. Various wireless technologies have been utilized for sensing, including Wi-Fi [1], [2], RFID [3], [4], LoRa [5], [6], mmWave [7], [8], and ultrasound [9], [10]. Among these, Wi-Fi sensing has gained significant attention owing to the widespread availability of Wi-Fi signals. Wi-Fi sensing has enabled a wide range of applications, such as human activity recognition [11], [12], vital sign monitoring [13]–[16], material identification [17] and object size measurement [18].

Although promising, Wi-Fi sensing has several fundamental issues which hinder its wide adoption in real-life scenarios. (i) The sensing range of Wi-Fi is very limited because it inherently relies on weak reflection signal from the target (i.e., human body). The state-of-the-art Wi-Fi sensing system, Farsense [19], achieves a maximum range of only 8 meters. (ii) The sensing performance of Wi-Fi sensing is highly dependent on the target's orientation. Existing Wi-Fi sensing approaches typically require the target to maintain a specific orientation (facing directly toward both the transmitter and receiver) to achieve good sensing performance [20]. When the target orientation changes, the fine-grained motion information (e.g., respiration pattern) cannot be captured.

In this paper, we present RISensing, a Wi-Fi-based sensing system that leverages Reconfigurable Intelligent Surfaces (RIS) to address these fundamental issues, moving Wi-Fi sensing one step closer to real-life adoption. Specifically, as shown in Figure 1(b), we introduce an RIS to create a new target reflection signal (i.e., signal reflected once by the RIS and once by the target), as highlighted in red. Unlike existing Wi-Fi sensing systems which rely on only one reflection as shown in Figure 1(a), reflected by the target and reaching the receiver without other intermediate reflections (as highlighted
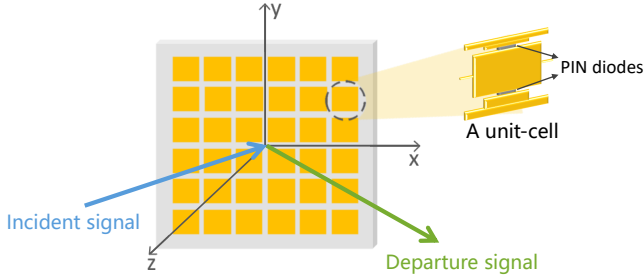
Figure 2: Principle of RIS.

in blue), we smartly combine the direct target reflection and the newly created RIS-based target reflection to capture human motion. Employing the RIS-based target reflection for Wi-Fi sensing provides the following benefits.

- By constructively combining the RIS-based target reflection signal and direct target reflection signal, we are able to improve the overall signal strength of target reflection signal, significantly improving the sensing range.
- The RIS-based target reflection signal and direct target reflection signal present multiple sensing views from different orientations with respect to the target. With these two different signals, we eliminate the need for the target to maintain a specific orientation, and the signal variations captured from different views greatly enhance the robustness of Wi-Fi sensing. For instance, as shown in Figure 1(a), the direct reflection signal (highlighted in blue) is reflected by the side of human chest, resulting in minimal signal variation due to limited displacement during respiration, and correspondingly poor sensing performance. In contrast, as shown in Figure 1(b), by deploying an RIS, the reflected signal can originate from the front of chest, where the displacement during respiration is much larger and the corresponding signal variation is more clearer. By combining these two different reflections, we can make Wi-Fi sensing more robust in real-world scenarios.

To effectively leverage RIS for Wi-Fi sensing, we first characterize the RIS-based target reflection signal. Specifically, we model the power of signal generated by RIS, and validate that the signal reflected by RIS has larger power than the direct target reflection. Different from direct target reflection, whose power depends on two distances, i.e., transmitter-target distance and target-receiver distance, the RIS-based reflection signal power is determined by three distances: transmitter-RIS distance, RIS-target distance and target-receiver distance. The longer propagation distance results in weaker signal power of RIS reflection. To compensate for this and significantly improve the signal power, the RIS leverages hundreds of unit-cells to reflect Wi-Fi signals as shown in Figure 2, and employs beamforming to focus the reflected signal toward the target.

In this paper, we propose to constructively combine the RIS-based target reflection signal and direct target reflection signal to significantly boost the sensing performance. This can be achieved by tuning the phase of RIS-based target reflection signal to align with that of direct target reflection. While this is a promising technique, two key challenges need to be tackled to implement this approach in a functional system.

- First, it is difficult to change the phase of RIS-based target reflection signal in a fine-grained granularity. This occurs because RIS employs many unit-cells to generate the reflection signal, and each unit-cell is equipped with two PIN diodes to tune its phase shift, but with limited phase tuning resolution [21], [22].) Specifically, each programmable unit-cell employed in our system typically supports only four discrete phase shifts (i.e., 0°, 90°, 180° and 270°) [22], resulting in coarse phase adjustments.
- Second, the phase of direct target reflection signal is unknown. A straightforward approach is to try all the possible phase shifts of RIS-based target reflection signal (0°~360°) and identify the one that yields the best sensing performance. The best sensing performance is achieved when the phase of RIS-based target reflection signal is changed to be the same as that of direct target reflection signal. To determine whether the best performance is achieved or not, for each phase shift, we need to collect the received signal over a period (e.g., 3 s) during target movement to check the target-induced signal amplitude variation. However, this process is quite time-consuming and the time delay can be as large as tens of minutes, making it impractical for real-time applications.

To achieve fine-grained phase tuning (i.e., with a granularity of 1°) of RIS-based target reflection signal, we smartly leverage the combination effect of multiple RIS unit-cells. In our design, the RIS consists of 16×16 unit-cells, and each unit-cells reflects Wi-Fi signal. The RIS-based target reflection signal is a combination of signals reflected by these unit-cells. Even though each unit-cell can only support four discrete phase shifts, we observe that by carefully configuring different phase shifts across these unit-cells, we can effectively change the phase of RIS-based target reflection signal in a much finer granularity. To determine the optimal phase shift combination of these unit-cells for the desired RIS-based target reflection signal's phase change, we adopt the Particle Swarm Optimization (PSO) algorithm [23].

To significantly reduce the time delay when searching for the desired phase change of RIS-based target reflection signal, we propose a novel method based on two key observations. Our basic ideas are (i) to significantly reduce the search space from hundreds of candidates to just a few, and (ii) to minimize the required number of signal collection periods to just one.

Observation I. When we vary the phase shift of RIS-based target reflection signal, the sensing performance varies following a sine-wave pattern. The optimal sensing performance is achieved when the phase of RIS-based target reflection signal is tuned to be exactly the same as that of direct target reflection signal. We observe that the relationship between the sensing performance and the phase shift of RIS-based target reflection signal demonstrate a sine-wave pattern. Therefore, instead of exhaustively searching all the possible phase shifts (i.e., 360 values), we propose to sample only a subset of the phase shift space (i.e., 8 values) and leverage the sine-wave pattern to efficiently estimate the optimal one.

Observation II. We leverage one observation to further reduce the latency: the target movements are typically at low frequencies (≤ 20 Hz) while the sampling rate of Wi-

Fi receiver is much higher (e.g., 2000 Hz). Thus, the signals sampled at the close-by timestamps contain the same target movement information. By sub-sampling the received signals in the time domain, we obtain multiple groups of signal samples containing the same target movement information. For each group, we adjust the phase shift of RIS-based target reflection signal. As mentioned earlier, the sine-wave curve generation requires 8 distinct phase changes. Initially, for each phase change, we need to sample the received signal for 3 s to evaluate sensing performance, resulting in a total latency of 24 s. However, based on the observation, we do not need to sample the received signals for each phase change separately, but we can sample the received signals for all 8 phase changes at the same time within the same 3 s window. This reduces the total latency from 24 s to just 3 s.

Contributions. The main contributions of RISensing are summarized as follows.

- To the best of our knowledge, we study the feasibility of leveraging Reconfigurable Intelligent Surfaces to address two fundamental issues (i.e., limited sensing range and orientation-dependent issue) of Wi-Fi sensing for the first time. Unlike prior Wi-Fi sensing systems which rely on a single direct target reflection signal, we leverage two target reflection signals to boost the sensing performance.
- We characterize the RIS-based target reflection signal for sensing, and propose an RIS-based sensing model. Additionally, we design novel signal processing methods to address two challenges when constructively combining the RIS-based and direct target reflection signals.
- We implement RISensing using commodity Wi-Fi devices and an RIS which consists of 16×16 unit-cells with a total size of 0.35×0.35 m^2. The experiment results demonstrate that RISensing can significantly improve the sensing range from 4 m to 23 m, and mitigate the orientation-dependent issue.

II. RELATED WORK

In this section, we introduce the prior work closely related to RISensing.

RF-based wireless sensing. RF-based wireless sensing technologies have enabled many appealing applications, ranging from coarse-grained activity recognition [11], [12], keystroke identification [24], [25], and hand gesture recognition [26]–[29] to fine-grained vital sign monitoring [13]–[16], [30]. Although promising, existing Wi-Fi sensing systems have two fundamental issues: limited sensing range and sensitivity to target orientation [20], [31]. The short sensing range primarily stems from the weak signal reflections from the human body, which fundamentally restricts the sensing coverage. Moreover, most Wi-Fi sensing systems rely on the assumption that the target maintains a fixed orientation to the transmitter and receiver, which have a poor sensing performance when the target changes orientation. These limitations pose significant challenges for deploying Wi-Fi sensing in real-world scenarios.

To address the limited sensing range, FarSense [19] computes the ratio of CSI values from two antennas at the

(a) A scenario of Wi-Fi sensing   (b) The vector representation of signal
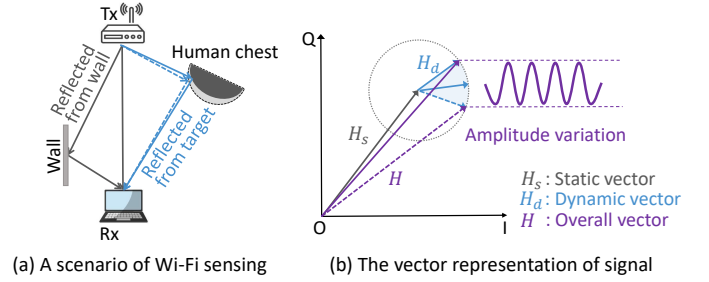
Figure 3: Prior Wi-Fi sensing model.

receiver, which effectively eliminates both amplitude noise and phase offset of CSI. By a joint utilization of CSI amplitude and phase, FarSense extends the sensing range to 8 m. Building upon this, EMA [16] employs multi-antenna beamforming to further enhance the sensing distance to 11 m. Diversense [32] integrates signals from 30 subcarriers of 3 antennas at the receiver to improve the sensing range. Compared with FarSense [19] and EMA [16], RISensing achieves longer sensing range (23 m). Moreover, RISensing smartly addresses the orientation-dependent issue for wireless sensing, which is not explored in Diversense [32], FarSense [19] and EMA [16].

RIS-based sensing. The emerging RIS technology is promising for wireless sensing. RFlens [21] improves the respiration sensing performance under non-line-of-sight (NLoS) scenarios via RIS beamsteering. LLAMA [33] utilizes RIS to enhance the reflected signal by polarization matching, which enables the respiration detection even with low transmission power. Moreover, researchers also leverage RIS to enable multi-target respiration sensing [34]–[36]. Different from these works which overlook the direct target reflection signal [34]–[36] or make the direct reflection signal negligible [21], RISensing constructively combines the RIS-based target reflection signal with the direct target reflection signal to address two fundamental issues, i.e., limited sensing range and orientation-dependent issue.

RIS-based localization. MetaRadar [37] and Meta2Locate [38] use an RIS to assist RSS fingerprint-based indoor localization. MetaSight [39] employs multiple RISs to localize objects under the NLoS scenario. RIScan [40] leverages RIS to perform Wi-Fi beam scanning for parallel multi-user indoor localization. Different from these works that utilize RIS for localization, we focus on a different research topic, i.e., RIS-based wireless sensing.

III. PRELIMINARY

A. Prior Wi-Fi Sensing Model

Wi-Fi signals propagate from the transmitter to receiver through multiple paths, as shown in Figure 3(a). The overall Channel State Information (CSI) $H(f,t)$, which characterizes the wireless channel [41], can be expressed as $H(f,t) = \frac{Y(f,t)}{X(f,t)}$, where $X(f,t)$ and $Y(f,t)$ represent the transmitted and received signals, f denotes the subcarrier frequency and t is the timestamp. We divide these signals into two groups: static signal and dynamic signal. The static signals consist of the line-of-sight (LoS) signal between the transmitter and

(a) A scenario of RIS-based Wi-Fi sensing

(b) The combination of two dynamic reflection signals

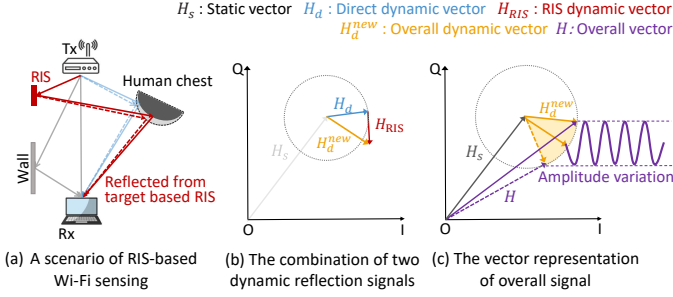(c) The vector representation of overall signal

Figure 4: Our RIS-based Wi-Fi sensing model.

receiver, and the signals reflected from static objects such as walls. The dynamic signal represents the signal reflected from the moving target. We employ $H_s(f,t)$ and $H_d(f,t)$ to represent the channels of static path and dynamic path, respectively [41]. The overall CSI can be rewritten as

$$
\begin{aligned}
H(f,t) &= H_s(f,t) + H_d(f,t) \\
&= H_s(f,t) + A(f,t)\, e^{j\frac{2\pi d(t)}{\lambda}},
\end{aligned} \tag{1}
$$

where $d(t)$ represents the propagation path length of dynamic signal which changes with the target movement, λ is the wavelength, and $A(f,t)$ is the complex attenuation.

The relationship between the target movement and amplitude variation is presented in Figure 3(b). We illustrate the static and dynamic channels in the I/Q vector space, where the length of the vector represents the amplitude, and the angle between the vector and the I-axis represents its phase. The overall vector H is the sum of dynamic vector H_d and static vector H_s. The overall vector represents the CSI which is retrieved from the Wi-Fi receiver, and we utilize the amplitude of CSI to capture target movement. During the target movement, the static vector H_s does not change, while the dynamic vector H_d changes. For example, for the respiration sensing with a chest displacement of around 5 mm, the dynamic vector H_d rotates $60°$ with respect to the static vector, inducing the amplitude of overall vector to change.

B. RIS-based Target Reflection Signal Generation

An RIS consists of M unit-cells where each unit-cell is equipped with two PIN diodes to change the phase shift. Each unit-cell receives and reflects the signals from Wi-Fi transmitter, and the combination of these reflected signals forms the overall RIS signal. To utilize RIS signal for sensing, we focus the RIS signal toward the target via beamforming [21], [22]. Specifically, by identifying the direction where the target is located, we can configure the unit-cells to generate an RIS signal toward that direction. As a result, the power of RIS-based target reflection signal is directly affected by the number of unit-cells. A large number of unit-cells can generate a stronger RIS-based target reflection signal. In our design, we employ an RIS comprising 16×16 unit-cells (a total of 256), which enables a large beamforming gain.

IV. RIS-BASED SENSING MODEL

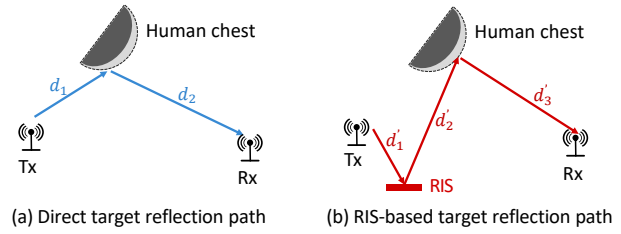In this section, we introduce the RIS-based sensing model which involves two dynamic signals (i.e., target reflection

(a) Direct target reflection path

(b) RIS-based target reflection path

Figure 5: Analyzing direct target reflection signal and RIS-based target reflection signal.

signals)[1]. This model can guide the design of RIS-based sensing systems.

A. Modeling Received Signal with RIS

Different from the prior Wi-Fi sensing model which involves only one dynamic signal, our sensing model includes two dynamic signals, i.e., direct target reflection signal and RIS-based target reflection signal. The overall CSI can be represented as

$$
H(f,t) = H_s(f,t) + H_d(f,t) + H_{RIS}(f,t), \tag{2}
$$

where $H_{RIS}(f,t)$ represents the channel of RIS-based target reflection signal. Both dynamic components contain the target information, and induce the overall CSI to vary. As shown in Figure 4(a), when we introduce an RIS into the sensing scenario, the transmitted signal reaches the receiver through two dynamic paths, including the direct reflection from the target and an RIS-based reflection. Figure 4(b) illustrates the vector representation in the complex I/Q vector space. The direct dynamic vector H_d (highlighted in blue) and the RIS dynamic vector H_{RIS} (highlighted in red) are combined to form a new dynamic vector H_d^{new}. The overall dynamic signal H_d^{new} varies with the target movement and combines with the static vector H_s at the receiver, resulting in the amplitude variation of the overall signal vector H for sensing as shown in Figure 4(c).

B. Modeling Direct Target Reflection Signal

The direct reflection path can be divided into two segments (i.e., TX→Target and Target→RX) as shown in Figure 5(a). d_1 and d_2 represent the transmitter-target distance and target-receiver distance, respectively. By applying the Friis equation [42] to the first part (TX→Target), we can obtain the signal power arriving at the target as

$$
P_{tx \to tar} = P_T G_T \cdot \frac{1}{4\pi (d_1)^2} = \frac{P_T G_T}{4\pi (d_1)^2}, \tag{3}
$$

where P_T is the transmission power and G_T is the antenna gain of the transmitter. The signal reflected by the target reaches the receiver (Target→RX), and the power P_d of direct target reflection signal at the receiver can be represented as

$$
P_d = P_{tx \to tar} \cdot \sigma \cdot \frac{1}{4\pi (d_2)^2} \cdot A_R = \frac{P_T G_T \sigma A_R}{(4\pi)^2 (d_1 d_2)^2}, \tag{4}
$$

where σ is the Radar Cross Section (RCS) of target. $A_R = \frac{G_R \lambda^2}{4\pi}$ where G_R is the antenna gain of the receiver and λ is

---

[1] We use target reflection signal, dynamic signal, and dynamic vector interchangeably in this paper.

H_s : Static vector H_d : Direct dynamic vector H_{RIS} : RIS dynamic vector H_d^{new} : Overall dynamic vector H : Overall vector

(a) The direct reflection signal   (b) Random combination of two reflection signals   (c) Constructive combination of two reflection signals
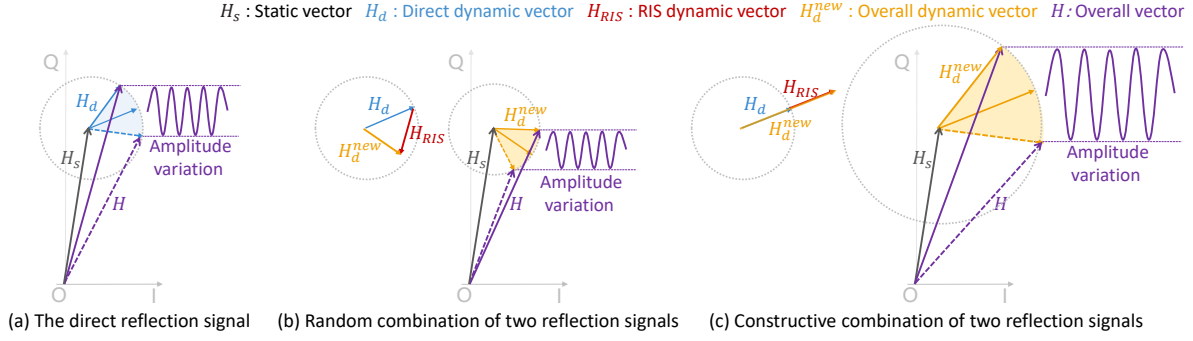
Figure 6: Combination of the RIS-based target reflection signal and the direct target reflection signal.

the signal wavelength. Therefore, the power of direct target reflection signal is determined by the product of two distance segments $d_1 d_2$.

C. Modeling RIS-based Target Reflection Signal

Different from the direct target reflection signal which only involves two distance segments, the RIS-based target reflection signal is divided into three segments: transmitter-RIS distance d_1', RIS-target distance d_2' and target-receiver distance d_3' as shown in Figure 5(b). The signal power arriving at the RIS (i.e., TX→RIS) can be expressed as

$$P_{tx \to RIS} = P_T G_T \cdot \frac{1}{4\pi \left(d_1'\right)^2} = \frac{P_T G_T}{4\pi \left(d_1'\right)^2}, \quad (5)$$

where P_T is the transmission power and G_T is the antenna gain of the transmitter. Then we model the signal power arriving at the target, i.e., RIS→Target, as

$$P_{RIS \to tar} = P_{tx \to RIS} \cdot G_{RIS} \cdot \frac{1}{4\pi \left(d_2'\right)^2} = \frac{P_T G_T G_{RIS}}{4\pi^2 \left(d_1' d_2'\right)^2}, \quad (6)$$

where G_{RIS} represents the beamforming gain of RIS, which is determined by the number of unit-cells. Finally, for the third part, i.e., Target→RX, the power of RIS-based reflection signal at the receiver can be expressed as

$$P_{RIS} = P_{RIS \to tar} \cdot \sigma \cdot \frac{1}{4\pi \left(d_3'\right)^2} \cdot A_R = \frac{P_T G_T G_{RIS} \sigma A_R}{4\pi^3 \left(d_1' d_2' d_3'\right)^2}, \quad (7)$$

where σ is the RCS of target. $A_R = \frac{G_R \lambda^2}{4\pi}$ where G_R is the antenna gain of the receiver and λ is the signal wavelength. Now we observe that the power of RIS-based target reflection signal is determined by the product of three distances $d_1' d_2' d_3'$.

Power comparison between two target reflection signals. Now we compare the power of these two target reflection signals. The RIS-based target reflection signal propagates a longer path than the direct target reflection signal, resulting in much larger signal attenuation. If the power of RIS-based target reflection signal is comparable to that of direct reflection signal, we are able to effectively leverage the RIS to boost the sensing performance.

The power of RIS-based target reflection signal is inversely proportional to the square of the product of three distances, whereas the direct target reflection signal power is inversely proportional to the square of the product of two distances. The

power ratio between these two target reflection signals can be expressed as

$$\frac{P_{RIS}}{P_d} = \frac{(d_1 d_2)^2}{4\pi (d_1' d_2' d_3')^2} \cdot G_{RIS}. \quad (8)$$

Based on the power ratio, we analyze the power of two target reflection signals.
1) Based on our empirical experiments, the beamforming gain G_{RIS} can be as large as 6 dBi.
2) d_2 in the direct target reflection path is almost identical to d_3', i.e., $d_2 \approx d_3'$. This is because both of them represent the distance between target and receiver, as shown in Figure 5(a) and (b).
3) To minimize the product $d_1' d_2'$ of the transmitter-RIS distance d_1' and RIS-target distance d_2' in the RIS-based reflection path (Figure 5(b)), we deploy the RIS as close as possible, e.g., 0.5 m, to the transmitter.

As a result, the power of RIS-based target reflection signal can be larger than that of direct target reflection signal. Our empirical experiments demonstrate that the power of RIS-based target reflection signal can reach up to 2.5 times that of direct target reflection signal, i.e., $P_{RIS} = 2.5 P_d$.

V. SYSTEM DESIGN

In this section, we illustrate the system design of RISensing. Our key idea is to make the two target reflection signals constructively combine to improve the sensing range and address the orientation-dependent issue, as illustrated in Section V-A. To achieve this, we propose to change the phase of RIS-based target reflection signal to align with that of direct target reflection signal. Note that the phase of direct target reflection signal cannot be controlled while that of the RIS-based target reflection signal is programmable. However, there are two challenges as described below.

- The first challenge is how to tune the phase of RIS-based target reflection signal with a fine-grained granularity. Specifically, the unit-cells of RIS support only four discrete phase shifts, making it difficult to achieve the desired phase adjustment accurately. We address this issue in Section V-B.
- The second challenge is the unknown phase of direct target reflection signal. We have to try all the possible phase shifts and search for the optimal one, leading to very high latency. We explain how to significantly minimize the latency and achieve real-time human sensing in Section V-C.
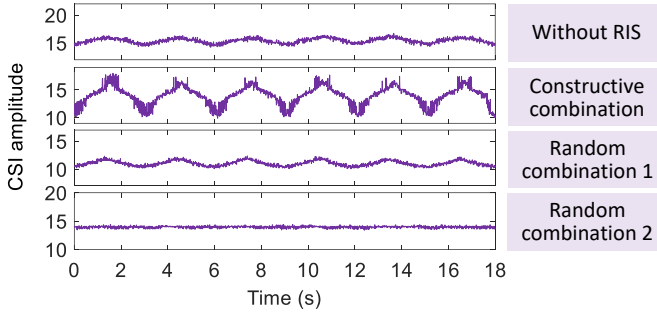
Figure 7: Respiration-induced CSI amplitude variations under different combinations of two target reflection signals.

(a) The phase change of RIS reflection signal is $45°$

(b) The phase change of RIS reflection signal is $72°$

Figure 8: Leveraging the phase shift combination of multiple unit-cells to fine-tune the phase of RIS-based reflection signal.

A. Constructive Combination of Two Target Reflection Signals

In this section, we explain the benefits of constructively combining the two target reflection signals.

Random combination of two reflection signals. As shown in Figure 6(b), where the signals are represented in the I/Q vector space, the two reflection signals, i.e., direct target reflection signal H_d (highlighted in blue) and RIS-based target reflection signal H_{RIS} (highlighted in red), are typically combined randomly at the receiver. The random combination results in unpredictable sensing performance and can even cause performance degradation. Note that we employ CSI amplitude variation to quantify the sensing performance, and a larger CSI amplitude variation indicates better sensing performance. By comparing Figure 6(a) (without RIS) to Figure 6(b) (with RIS), we observe that the RIS-based target reflection signal can cause CSI amplitude variation to be smaller. This is because the RIS-based target reflection H_{RIS} is not constructively combined with the direct target reflection signal H_d, and the amplitude of overall target reflection signal H_d^{new} is reduced. This occurs when the phase difference between the two reflection signal vectors falls within the range of $[-90°, 90°]$.

Constructive combination of two reflection signals. In contrast, the constructive combination of the two target reflection signals can significantly improve the sensing performance. As presented in Figure 6(c), when the phase of RIS-based target reflection signal H_{RIS} is exactly the same as that of the direct target reflection signal H_d, these two reflection signals are constructively combined and the overall target reflection signal is maximized. This constructive combination results in the largest amplitude variation, and consequently the optimal sensing performance. With the maximum amplitude of overall target reflection signal, the sensing range can be significantly improved. In addition, the RIS-based target reflection signal and direct target reflection signal present multiple sensing views from different orientations with respect to the target. When the direct target reflection signal alone does not provide a clear amplitude variation for sensing, we can still leverage the RIS-based target reflection signal to enlarge the overall amplitude variation.

Benchmark experiments. We conduct experiments to verify the effect of RIS on respiration sensing. We mainly pay attention to the combination of two target reflection signals. In the experiments, we set the transmitter-RIS distance as
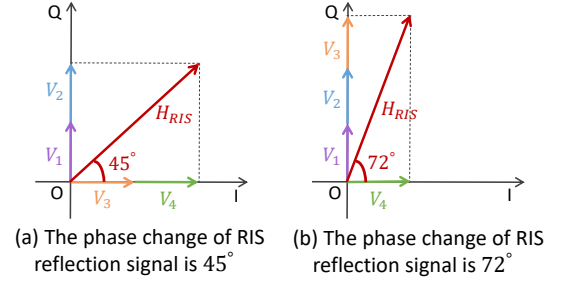
0.3 m and transmitter-receiver distance as 3 m. The target sits in a chair and breathes normally. By generating different RIS-based target reflection signals, we vary the combination of two target reflection signals. Figure 7 shows the CSI amplitude variation induced by respiration under different path combinations. We observe that when the two target reflection signals constructively combine, the CSI amplitude variation induced respiration is more significant. In contrast, when the two target reflection signals randomly combine, the respiration-induced CSI amplitude variation remains unchanged or becomes smaller, compared to that without RIS. Therefore, to improve sensing performance, we aim to achieve constructive combination of the two target reflection signals.

B. Tuning Phase in Fine-grained Granularity

We adjust the phase shifts of RIS unit-cells to change the phase of RIS-based target reflection signal. However, each RIS unit-cell supports only four discrete phase shifts (i.e., $0°$, $90°$, $180°$ and $270°$) [22]. This limited resolution makes it difficult to finely tune the phase of RIS-based target reflection signal. For example, if a $41°$ phase adjustment is needed, which is not supported by the available discrete phase shifts, we cannot achieve constructive combination.

Fortunately, we observe that by carefully configuring different phase shifts across multiple RIS unit-cells, we can effectively change the phase of RIS-based target reflection signal in a much finer granularity. A simple example is shown in Figure 8 where the RIS consists of four unit-cells. Each vector V_n (n = 1, 2, 3 and 4) represents the signal reflected from a unit-cell in the I/Q vector space. The angle between each vector and I-axis represents its new phase shift. The initial phase shift of each vector is $0°$. Suppose the desired phase shift of RIS reflection signal H_{RIS} is $45°$. As shown in Figure 8(a), by configuring the phase shifts of two unit-cells to $0°$ and the other two to $90°$, we can induce the phase of RIS-based target reflection signal H_{RIS} to change by $45°$. Similarly, as shown in Figure 8(b), by configuring three unit-cells with a phase shift of $90°$ and the remaining one unit-cell to $0°$, we can tune the phase of RIS-based target reflection signal by $72°$. As a result, by combining the phase shifts of multiple RIS unit-cells, we can change the phase of RIS-based target reflection signal with a much finer granularity. Given that our RIS consists of 16×16 unit-cells, this approach allows us to achieve a phase adjustment granularity as small as $1°$.

Now we analyze the relationship between the phase shift combination of unit-cells and the phase change of RIS-

based target reflection signal. The mathematical relationship is expressed as

$$e^{j\Delta\Phi_{RIS}}H_{RIS} = \sum_{n=1}^{N} V_n e^{j(\Delta\phi_n)}, \qquad (9)$$

where V_n and $\Delta\phi_n$ represent the signal of the nth unit-cell and its phase shift. H_{RIS} denotes the original RIS-based target reflection signal, and $\Delta\Phi_{RIS}$ stands for its phase change. Since there are 256 (16 × 16) unit-cells and each unit-cell has 4 possible discrete phase shifts, there are 4^{256} phase shift combinations. It is not possible to check all of these combinations. We observe that multiple phase shift combinations can lead to an identical phase change of RIS-based target reflection signal. Therefore, we just find one of these combinations to reduce the latency and effort. Specifically, we create a matching table which shows one phase shift combination of unit-cells for each phase change of RIS-based target reflection signal. Once this table is established, we can efficiently determine the appropriate phase shift combination for fine-grained phase tuning of RIS-based target reflection signal. More importantly, this table is constructed only once before we sense human motion.

Now we explain how to efficiently construct the matching table. In this table, we derive one phase shift combination of all the RIS unit-cells for each phase change of RIS-based target reflection signal. To derive one combination for a specific phase change, we adopt the Particle Swarm Optimization (PSO) algorithm [23]. The PSO algorithm is inspired by the behavior of bird swarm, whose key idea is to iteratively adjust the position of each "bird" in the search space, allowing the swarm to progressively search for and converge toward the global optimal solution. In our design, each "bird" represents a combination of all RIS unit-cell phase shifts, i.e., $\boldsymbol{\Delta\phi} = [\Delta\phi_1, \Delta\phi_2, \Delta\phi_3, \ldots, \Delta\phi_n]$. The phase change of the RIS-based target reflection signal generated by this combination is the position of "bird" in the search space.

The details about applying PSO to achieve the optimal phase shift combination are shown below.

- **Initialization.** We initialize the number of "birds" (i.e., the phase shift combinations of all RIS unit-cells $\boldsymbol{\Delta\phi}$) to $N_{bird} = 50$ based on our empirical experiments. Our objective is to search for the optimal phase shift combination, and the process terminates once one of these "birds" achieves it. To balance exploration and prior knowledge, half of these combinations are generated randomly, while the other half follow the RIS beamforming method described in Section III-B.
- **Fitness function.** We define a fitness function [43] to evaluate the quality of each bird's current position, which measures how closely the phase shift combination of each bird approaches the desired phase shift combination. Specifically, the fitness function is defined as the squared difference between the phase change of the RIS-based target reflection signal $\Delta\Phi_{RIS}$ and the desired phase change $\Delta\Phi_{RIS}^{goal}$:

$$F_{fit} = \left(\Delta\Phi_{RIS} - \Delta\Phi_{RIS}^{goal}\right)^2, \qquad (10)$$
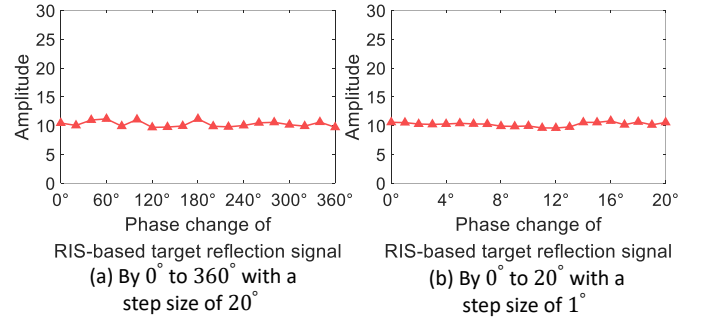

Figure 9: Fine-tuning the phase change of RIS-based target reflection signal.

where $\Delta\Phi_{RIS}$ can be derived from a bird's current phase shift combination via Equation (9). The smaller value of F_{fit}, the current phase shift combination is closer to the desired one.

- **Iteration.** We evaluate whether any of the 50 "birds" (phase shift combinations) achieves the optimal solution based on the fitness function. If none are optimal, we update the position of each "bird" and re-evaluate. This process repeats iteratively until the optimal phase shift combination is achieved. Now we explain how to update the position of each "bird". First, we select the "bird" (i.e., phase shift combination) among 50 "birds", which is closest to the optimal combination. Second, we compare the bird's current position and previous position in the last step, and identify the one which is closer to the optimal phase shift combination. We employ these two pieces of information to compute an updated position of the "bird" [23].

The computation complexity of PSO algorithm is $\mathcal{O}(N_{bird} \cdot N \cdot T)$, where N_{bird} represents the size of "bird" swarm (set as 50 in our implementation), N denotes the problem dimension, i.e., the number of RIS unit-cells (256), and T is the number of iterations (maximum 1000 times in our implementation). The PSO algorithm converges within 10 s on average under these settings. Note that even though the PSO algorithm is an iteration-based method, we apply PSO offline just once before performing sensing task.

Benchmark experiments. We conduct benchmark experiments to verify whether we can fine-tune the phase of RIS-based target reflection signal. During phase tuning, we check the CSI amplitude to ensure that the newly adjusted RIS-based target reflection signal maintains maximum signal power. If the CSI amplitude decreases, the newly applied phase shift for the RIS-based target reflection signal is not optimal. First, we change the phase of RIS-based target reflection signal by 0° to 360° with a step size of 20°. As shown in Figure 9(a), we observe that we can change the phase by 60°, 120°, 160°, 240° and 300°, which are not supported by the default phase shifts of the unit-cell. Moreover, we are able to maintain the maximum signal strength even during the fine-tuning process. Second, we change the phase of RIS-based target reflection signal by 0° to 20° with a step size of 1°. As shown in Figure 9(b), we observe that we can change the phase with a step size as small as 1°, while still maintaining the maximum signal strength.
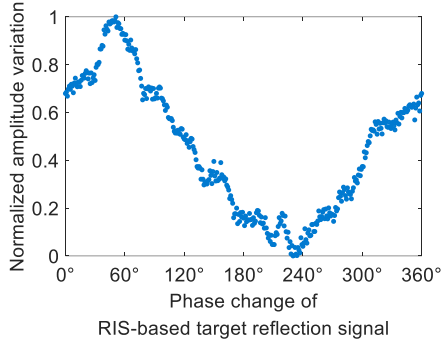
Figure 10: Sine-wave relationship between sensing performance and phase change of RIS-based target reflection signal.

C. Addressing Unknown Phase for Constructive Combination

To make the two reflection signals constructively combine, we propose to tune the phase of RIS-based target reflection signal, which is programmable, to be the same as that of direct target reflection signal. However, the phase of direct target reflection signal is unknown. A straightforward method is to try all the possible phase changes (i.e., $0° \sim 360°$), and search for the desired one that enables the best sensing performance. However, this simple approach can introduce latency significantly, making it impractical for real-time applications. Specifically, we employ the target-induced CSI amplitude variation as the metric for sensing performance to check whether the phase of RIS-based target reflection signal is changed to be the same as that of direct target reflection signal. The maximum target-induced CSI amplitude variation is achieved if the two phase values are the same. Therefore, for each search, we need to collect the received signal over a period (e.g., 3 s) during target movement to check the target-induced CSI amplitude variation. Given a search space of $[0°, 360°]$, the latency can be 360×3 s = 1080 s (18 min), which is unacceptable for real-time target sensing.

We significantly reduce the latency of the phase shift search process by leveraging two key observations, and the latency is minimized to just 3 s. Our basic ideas are (1) to significantly reduce the search space from hundreds of candidates to just a few, and (2) to minimize the required number of signal collection periods to just one.

Observation 1. *The relationship between sensing performance and the phase change of RIS-based target reflection signal demonstrates a sine-wave pattern.*

As shown in Figure 10, when we continuously change the phase of RIS-based target reflection signal with a granularity of $1°$, the sensing performance (i.e., the target-induced CSI amplitude variation) exhibits a sine-wave pattern. This occurs because the optimal sensing performance is achieved when the phase of RIS-based target reflection signal is tuned to be exactly the same as that of direct target reflection signal. As the RIS phase deviates from this optimal value, the sensing performance gradually degrades. When the RIS phase becomes exactly out of phase (i.e., $180°$ offset) with the direct reflection signal, the sensing performance reaches its minimum. As the phase continues to deviate away from this worst-case point, the sensing performance begins to improve again.
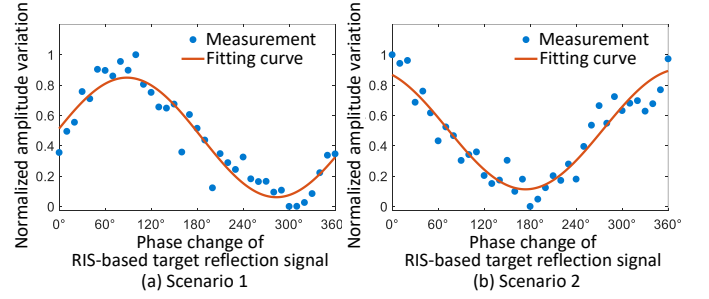

Figure 11: Sine-wave relationship between sensing performance and phase change of RIS-based target reflection signal.

Therefore, instead of exhaustively searching all the possible phase changes, we propose to sample only a subset of the phase shift space and leverage the sine-wave pattern to efficiently estimate the optimal phase change of RIS-based target reflection signal. Specifically, we vary the phase change from $0°$ to $360°$ with a step size of $10°$, and obtain the sensing performance at 37 points, as shown in Figure 11(a). We then apply the nonlinear least squares fitting method to obtain a smoothed curve (highlighted in red), which demonstrates a clear sine-wave pattern. The optimal phase change can be identified based on the peak of sine-wave curve. Moreover, while the location of peak (i.e., optimal phase change) can vary in different scenarios as shown in Figure 11(a) and (b), the sine-wave pattern remains stable. This method enables us to accurately identify the optimal phase change for RIS-based target reflection signal with much fewer measurements. As a result, the latency is reduced significantly. In our experiments, we use 8 phase changes to generate the sine-wave curve. Therefore, the latency is reduced from 360×3 s = 1080 s to 8×3 s, i.e., 24 s, where for each phase change, we collect received signal samples for 3 s to estimate the corresponding sensing performance (target-induced CSI amplitude variation).

We leverage the following observation to further reduce the latency. Specifically, the sine-wave curve generation requires 8 distinct phase changes. Initially, for each phase change, we need to sample the received signal for 3 s to evaluate sensing performance, resulting in a total latency of 24 s. However, we observe that we do not need to sample the received signals for each phase change separately, we can sample the received signals for all 8 phase changes at the same time within the same 3 s window. This reduces the total latency to just 3 s.

Observation 2. *The target movements are typically at low frequencies (i.e., ≤ 20 Hz), whereas the sampling rate at the Wi-Fi receiver is in the scale of kilohertz (e.g., 2000 Hz), which is hundreds of times higher.*

The human respiration rate is just $0.16 \sim 0.6$ Hz [19], [30], [31], which is much smaller compared to the signal sampling at the Wi-Fi receiver (e.g., 2000 Hz). Based on the observation described above, we propose to sub-sample the received signals in time domain, to obtain multiple groups of signal samples which contain the same target movement information. More importantly, for each group of signal samples, we vary the phase change of RIS-based target reflection signal and the number of groups of signal samples is exactly the same as that

(a) The overall received target-induced signal amplitude variation

(b) The signal samples of 8 phase changes by sub-sampling in the time-domain
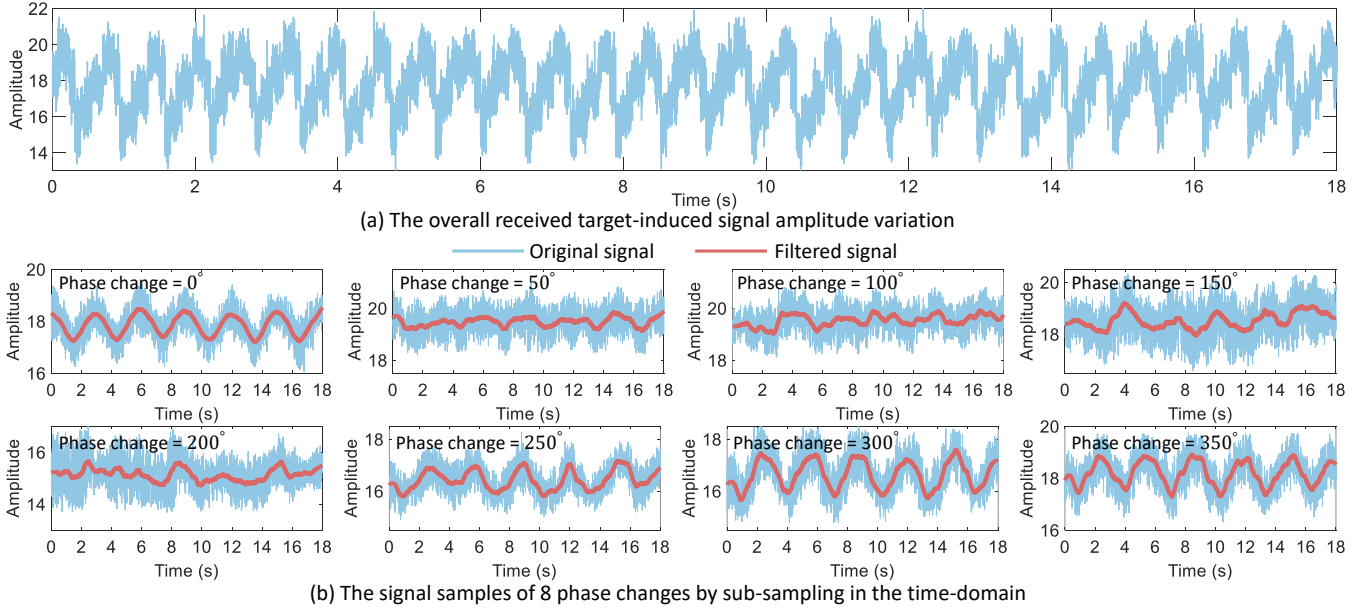
Figure 12: Extracting multiple signal samples corresponding to different phase changes from the same received target-induced signal amplitude variation.

(a) Dividing the received signal into multiple sub-sampling patterns

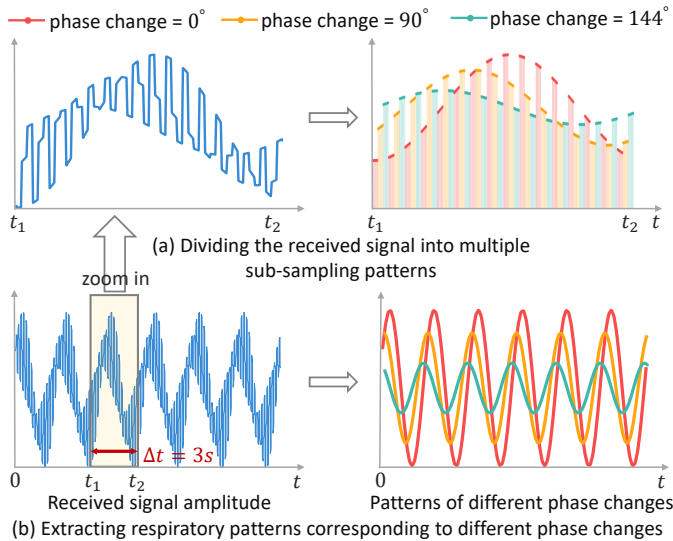(b) Extracting respiratory patterns corresponding to different phase changes

Figure 13: Time-domain sub-sampling for multiple phase changes of RIS-based target reflection signal.

of RIS phase change. As a result, by collecting the received signal once (i.e., for 3 s), we are able to obtain the multiple signal samples of different RIS phase changes to estimate the sensing performance.

One simple example with three phase changes is illustrated in Figure 13. As shown in Figure 13(a), when we sample the received signals during human respiration for 3 s, we periodically change the phase of RIS-based target reflection signal by three different values, i.e., $0°$, $90°$ and $144°$ (highlighted in red, orange and green). As a result, as shown in Figure 13(b), the overall respiration-induced CSI amplitude variation can be divided into three CSI amplitude variations based on the phase change. All these three CSI amplitude variations demonstrate the same respiration pattern, but with different phase changes of RIS-based target reflection signal. Therefore, by sampling the received signals only once, we can obtain the target-

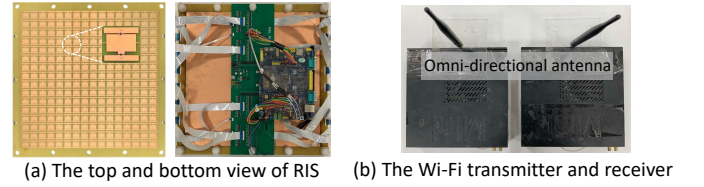(a) The top and bottom view of RIS   (b) The Wi-Fi transmitter and receiver

Figure 14: Hardware.

induced CSI amplitude variations for multiple phase changes at the same time. However, without such a design, we need to collect the received signals for multiple collection periods, each corresponding to a different phase change, in order to determine the optimal phase change.

Benchmark experiments. We conduct benchmark experiments to evaluate the effectiveness of sub-sampling the received signals for multiple phase changes. In the experiments, the transmitter-RIS distance and transmitter-receiver distance are set as 0.3 m and 3 m, respectively. The target sits 6 m from the transmitter and breathes normally. In the experiment, we choose the number of signal sub-sample groups as 8 and vary the phase changes with a step size of $50°$ from $0°$ to $360°$. Figure 12(a) presents the overall received target-induced signal amplitude variation over 18 s. By applying our method, we can obtain 8 respiration patterns corresponding to 8 different phase changes, as shown in Figure 12(b). We observe that when we vary the phase change of RIS-based target reflection signal, the sensing performance (i.e., respiration-induced CSI amplitude variation) varies significantly. Specifically, the respiration-induced CSI amplitude variation is worse at the phase change of $200°$. As the phase change is increased, the respiration-induced CSI amplitude variation becomes more obvious.

VI. IMPLEMENTATION

In this section, we introduce the implementation of RISensing, including RIS prototype, Wi-Fi transmitter and receiver, and data processing.
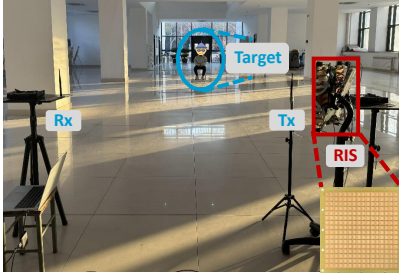
Figure 15: Default experiment scenario.

RIS prototype. Our RIS prototype operates at the 5 GHz frequency band with a bandwidth of 200 MHz (ranging from 5.15 GHz to 5.35 GHz), falling within the Wi-Fi spectrum. As shown in Figure 14(a), the RIS hardware consists of 16×16 unit-cells, and the overall size is 35×35 cm^2. Each unit-cell consists of two PIN diodes (SMP1340-040LF [44]). To independently adjust the phase shift of each unit-cell, we employ a microcontroller (i.e., STM32H743IIT6 from STMicroelectronics) and 64 SN74LV595 shift registers. We divide the 16×16 unit-cells into 16 groups and each group consists of 16 unit-cells with 32 PIN diodes. Each group is controlled by 4 shift registers which provide different DC voltages (0 V and 5 V) for the PIN diodes. By applying two different DC voltage levels to each PIN diode, we can obtain four states for each unit-cell, and correspondingly four discrete phase shifts (i.e., 0°, 90°, 180° and 270°). The microcontroller can reconfigure all the unit-cells within 0.6 ms and the overall power consumption of RIS is just in the milliwatt level.

Wi-Fi transmitter and receiver. We setup one pair of mini-computers equipped with Intel 5300 Wi-Fi NICs (Network Interface Card) as the transmitter and receiver, as shown in Figure 14(b). Both the transmitter and receiver are equipped with one omni-directional antenna. The central frequency of Wi-Fi transmitter and receiver is set as 5.24 GHz with a bandwidth of 20 MHz. The sampling rate of the receiver is set as 2000 Hz.

Data processing. We collect CSI data using the CSI tool developed by Halperin [45] and a laptop with a 2.3 GHz CPU (Intel i7-11800) and 16 GB memory for signal processing. After receiving the CSI, we first apply a Hampel filter [46] to denoise the raw CSI amplitude signals and then apply the Savitzky-Golay filter [47] to smooth the CSI amplitude. We calculate the autocorrelation coefficients of the processed CSI data across 30 subcarriers, to identify the most accurate subcarrier for sensing.

VII. Evaluation

In this section, we first evaluate the overall performance of RISensing in terms of sensing range, through-wall sensing capability, and its ability to address orientation-dependency issue. We then conduct comparison experiments with the state-of-the-art RIS-based sensing. Next, we evaluate the robustness of RISensing under different factors. Finally, we demonstrate the applicability of RISensing for gesture recognition.

Experimental scenarios and setup. We conduct comprehensive experiments in different indoor environments, including a corridor, an office and a laboratory. By default, we
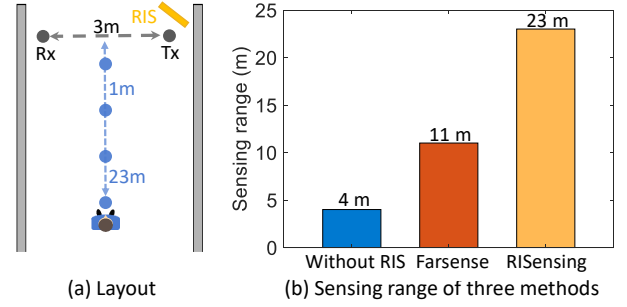

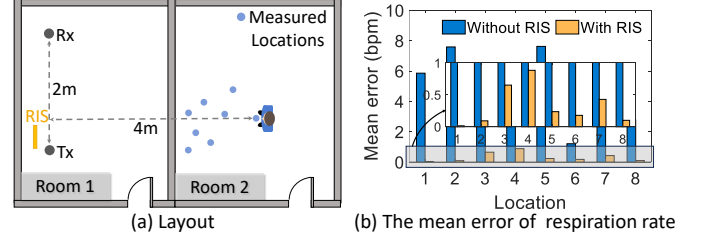Figure 16: Comparison between RISensing and two baseline methods.

Figure 17: Performance of through-wall sensing.

conduct experiments in the corridor environment as shown in Figure 15(a). We set the transmitter-RIS distance as 0.3 m and transmitter-receiver distance as 3 m. Both the antennas and RIS are deployed at a height of 1.1 m. For respiration monitoring, we recruit 12 targets (8 males and 4 females) with respiration rates ranging from 13 bpm (breaths per minute) to 25 bpm. To obtain the ground truth of respiration rate, we employ a respiration monitor belt logger sensor NUL-236 [48]. All the experiments have been approved by the Institutional Review Board (IRB).

Evaluation metric. For respiration sensing, we extract the respiration pattern and estimate the respiration rate for each measurement. To evaluate the respiration sensing performance, we calculate the mean respiration estimation error by comparing the estimated respiration rate against the ground truth.

A. Overall Performance

Improving sensing range. To evaluate the effectiveness of RISensing on improving sensing range, we conduct comparison experiments between RISensing and two baseline methods: (i) Wi-Fi sensing without RIS and (ii) the state-of-the-art Wi-Fi sensing, Farsense [19]. In the experiment, we set the transmitter-RIS distance as 0.3 m and transmitter-receiver distance as 3 m. We vary the target location from 1 m to 23 m with a step size of 1 m, along the perpendicular bisector of the transmitter-receiver line, as shown in Figure 16(a). Figure 16(b) shows the maximum sensing ranges for the three methods. Specifically, without RIS, we can only sense the target respiration up to 4 m, indicating the limited range of Wi-Fi sensing. The sensing range of Farsense is around 11 m. In contrast, RISensing achieves a sensing range of 23 m, significantly outperforming both the two baseline methods. The experiment results validate the effectiveness of RISensing in significantly extending the sensing range of Wi-Fi.

Enabling through-wall sensing. To evaluate the through-wall sensing capability of RISensing, we conduct experiments
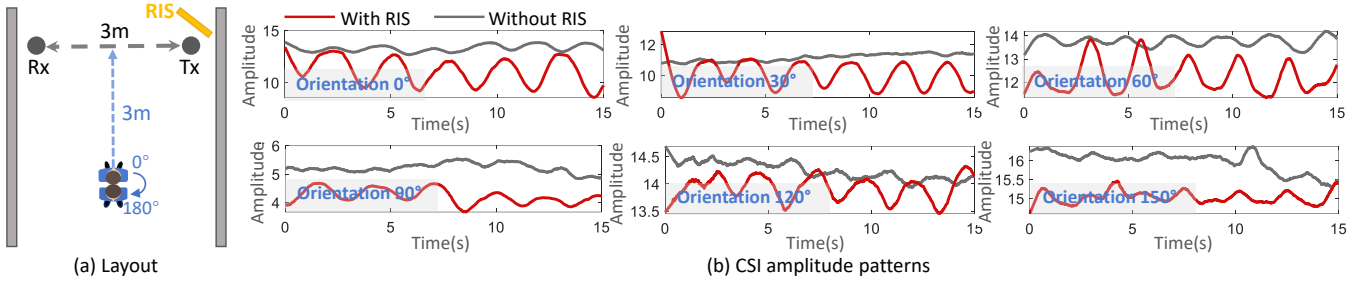
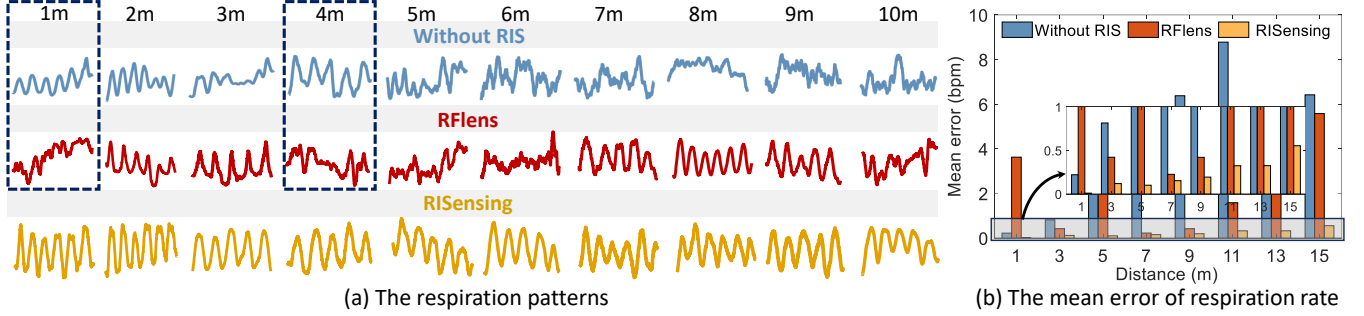Figure 18: CSI amplitude patterns under different target orientations.

Figure 19: Performance without RIS, RFlens and RISensing.

in the scenario as shown in Figure 17(a). The transmitter and receiver are placed in room 1 with a distance of 2 m. The target is located in room 2. We conduct experiments with and without RIS. Note that without RIS, we rely on direct target reflection signal for sensing, while with RIS, we combine RIS-based and direct target reflection signals for sensing. The target breathes normally at 8 locations with varying distances to transmitter and receiver. Figure 17(b) shows that RISensing can still accurately monitor respiration even through one wall and the respiration rate errors are below 1 bpm. However, without RIS, the respiration estimation errors are much larger than 1 bpm. Note that 1 bpm is the threshold for accurate respiration sensing [19]. The experiment results indicate that RISensing effectively enhances through-wall sensing capability.

Addressing the orientation-dependent issue. Prior Wi-Fi sensing typically suffers from strong orientation dependency issue and accurate sensing requires the target to face a specific direction. When the target changes orientation, the sensing performance can degrade significantly [19], [49]. To address this issue, we leverage RIS to improve the orientation robustness. Now we conduct experiments to evaluate the impact of different target orientations on respiration sensing. Specifically, we ask the target to rotate the body orientation while maintaining a fixed physical location as shown in Figure 18(a). For each orientation, we ask the target to breathe normally and extract the respiration patterns with and without RIS, respectively. As shown in Figure 18(b), we can observe that without RIS (highlighted in gray), the respiration pattern is clear at the orientation of $0°$. However, the respiration pattern becomes less distinct when the body orientation changes, especially at $90°$, $120°$ and $150°$. In contrast, when RIS is deployed (highlighted in red), the respiration pattern is always clear across different target orientations. This occurs because RIS provides an alternative signal path for Wi-Fi sensing, and effectively acts as an additional sensing view. When the direct target reflection is not available for sensing, the RIS-based

target reflection signal can be utilized to compensate for the direct one.

B. Comparison with State-of-the-art RIS-based sensing

In this section, we compare RISensing with the state-of-the-art RIS-based sensing, RFlens [21], which does not address the fundamental issues of wireless sensing, in terms of respiration sensing. During this experiment, we change the target location along the perpendicular bisector of the transmitter-receiver line from 1 m to 15 m with a step size of 1 m, as shown in in Figure 16 (a). For each target location, we conduct experiments under three different conditions: (i) without RIS, (ii) with RIS configured according to RFlens, and (iii) with RIS configured using our method.

Figure 19(a) shows the respiration patterns at $1\sim10$ m. We can observe that the sensing performance of RFlens varies significantly. While good performance (i.e., respiration-induced amplitude variation) is achieved at some distances, we cannot observe the respiration pattern at other distances. Moreover, the performance of RFlens can be worse than that without RIS, i.e., 1 m and 4 m, because of the random combination between the direct reflection signal and the RIS-based target reflection signal. In contrast, RISensing always achieves better performance, which benefits from the constructive combination of reflection signals.

Figure 19(b) shows the mean respiration rate estimation error. We observe when the target is located further away from the transmitter and receiver, the error increases. The error of RISensing is still less than 1 bpm at the distance of 15 m, while the mean error of RFlens is much larger and varies significantly with the target location. Even at target locations (i.e., 7 m and 9 m) where RFlens achieves lower error, RISensing still outperforms RFlens and has smaller errors. Without RIS, the error is much larger than 1 bpm even the distance is 5 m.
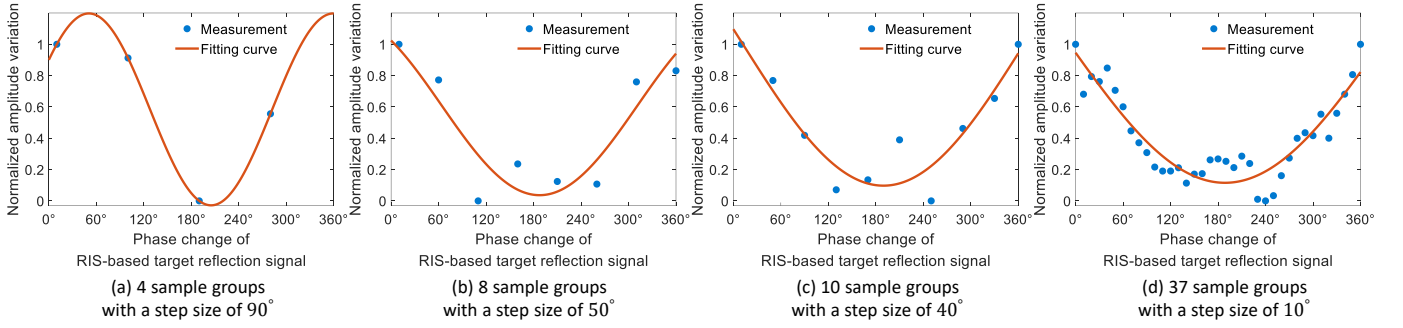
(a) 4 sample groups with a step size of 90°

(b) 8 sample groups with a step size of 50°

(c) 10 sample groups with a step size of 40°

(d) 37 sample groups with a step size of 10°

Figure 20: Combination of the RIS-based target reflection signal and the direct target reflection signal.

(a) Walking interference layout

(b) Standing/Leaping interference layout

(c) Walking interference

(d) Leaping interference

(e) Standing interference
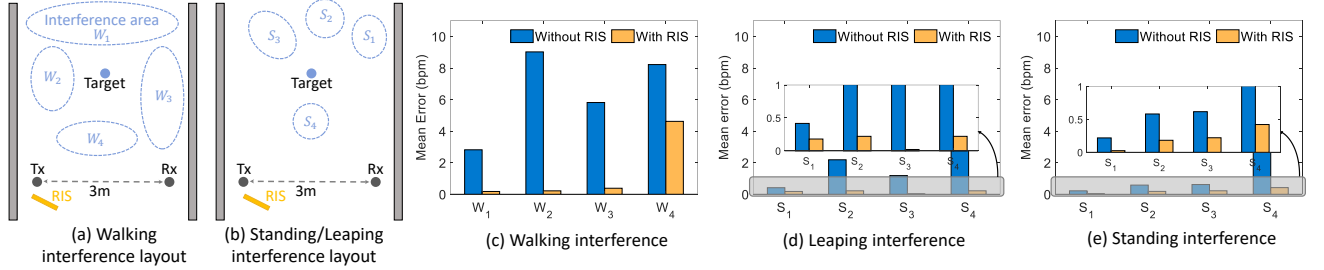
Figure 21: Performance under different interference.

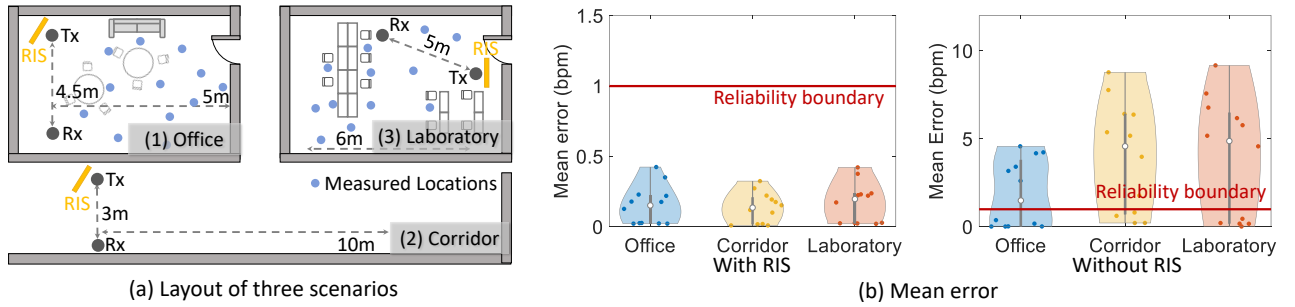(a) Layout of three scenarios

(b) Mean error

Figure 22: Performance under different environments.

C. Performance under Different Parameters

In this section, we evaluate the robustness of RISensing by varying different parameters.

Impact of the number of sub-sampling groups. We evaluate the impact of the number of sub-sampling groups on the performance of searching for the phase change. In this experiment, the transmitter-receiver distance is set as 3 m and the target is 8 m from the midpoint between the transmitter and the receiver. For all the experiments, the target breathes normally. We use four step sizes of the phase change from 0° to 360°: 90°, 50°, 40° and 10° for sub-sampling in time domain, resulting in 4, 8, 10 and 37 sample groups, respectively. Figure 20 shows the relationship between sensing performance (i.e., respiration-induced amplitude variation) and the phase change of RIS-based target reflection signal. Our measurement is highlighted in blue while the fitting sine-wave curve is highlighted in red. In general, the larger the number of sample groups, the more accurate the fitting sine-wave curve will be. However, we observe that when the number of sample groups is 8 in Figure 20(b), the fitting sine-wave curve is close to that in Figure 20(d) where the number of sample groups is 37. Therefore, in our experiments, we set the number of sample groups as 8, which can significantly reduce the delay of searching for the phase change.

Performance under different types of non-target interference. The non-target motion in the same environment can cause severe interference to target sensing. RISensing has the potential to mitigate non-target interference by controlling RIS-based signal toward the target. Specifically, RISensing can leverage RIS to significantly improve the target-induced signal variation, while the interferer-induced signal variation is not increased. In this case, the impact of non-target interference is mitigated.

We now evaluate the robustness of RISensing under different types of non-target interference, including walking, leaping and standing. In this experiment, we set the transmitter-receiver distance as 3 m and the transmitter-RIS distance as 0.5 m. The target sits 3 m away from the midpoint between the transmitter and the receiver. For each experiment, an interferer randomly walks, leaps or stands in the areas as highlighted in blue circles, as Figure 21(a) and (b) shown.

The experiment results are shown in Figure 21(c), (d) and (e), where we show the mean estimation error of respiration rate under three different types of interference. We observe that without RIS (highlighted in blue), the interference can significantly degrade the sensing performance of target sensing and result in very large respiration rate estimation errors. These respiration rate estimation errors are much larger than
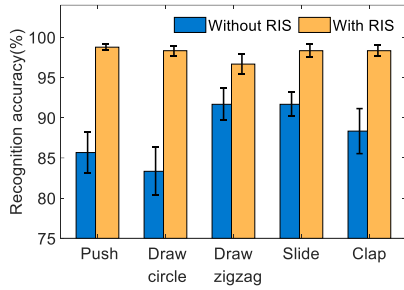
Figure 23: Performance of gesture recognition.

the threshold of 1 bpm, and thus they cannot be utilized for accurate respiration sensing. Moreover, the walking interference leads to the largest errors (i.e., 9 bpm), as shown in Figure 21(c). In contrast, RISensing can significantly mitigate the impact of these interference, and the respiration estimation errors (highlighted in yellow) are reduced. This is because RISensing can point the RIS-based signal toward the target to significantly improve the target-induced signal variation, while the interferer-induced signal variation is unchanged. Note that RISensing still has limitations in mitigating interference. Specifically, when the interferer is moving in the area of W_4 in Figure 21(a), the respiration estimation error is 5 bpm, which is larger than the threshold of 1 bpm. This is because when the interferer randomly walks within the area of W_4, it can block the target, and the large-scale motion of walking (on the meter level) significantly overshadows the tiny respiration of target, which occurs at the millimeter level.

Performance under different environments. To evaluate the performance of RISensing in different environments, we conduct experiments in three typical scenarios with different amount of multipath conditions: an office, a corridor and a laboratory, as shown in Figure 22(a). In each environment, we conduct respiration sensing experiments with the target located at 12 different locations, as highlighted in blue dots. As shown in Figure 22(b), the mean respiration rate estimation errors in the three environments are less than 1 bpm with RIS. In contrast, without RIS, the estimation errors increase significantly in all environments. In the corridor and laboratory scenarios, the respiration rate estimation errors exceed 5 bpm. The performance degradation is due to the longer distances between the target and the transmitter/receiver, which result in severe signal fading and interference, making it difficult to extract accurate respiration patterns. By enhancing the strength of the target reflection signal and suppressing irrelevant multipath, RISensing effectively improves the sensing accuracy. These experiment results demonstrate the robustness of RISensing in different multipath environments.

D. Gesture Recognition

To evaluate the capability of RISensing to enhance other sensing tasks, we apply RISensing to sense hand gestures. This experimental setup is the same as the default. We let targets stand 1.5 m away from the transmitter-receiver line and ask them to perform five gestures. We ask 15 targets to perform five different gestures (e.g., draw a circle, slide, draw a zigzag, push and clap), and collect 20 measurements for

each gesture. Figure 23 plots the results with and without the RIS. We observe that the average gesture recognition accuracy is increased from 83% to 96% when the RIS is applied. This result demonstrates that RISensing is effective in the gesture recognition task. This is because RISensing can amplify the gesture-induced signal variations, thus improving the recognition accuracy.

VIII. DISCUSSION

Moving target scenario. RISensing is effective for respiration sensing and gesture recognition only when the human target is stationary, such as sitting in a chair. When the target is walking or running, we are not able to capture the respiration or gesture information. This is because the signal variations induced by large-scale walking and running are much larger than those induced by respiration and gestures. As a result, the subtle signal variations induced by respiration or gestures are overwhelmed and buried in the larger motion-induced signal variations. It is very challenging to recover these tiny signal variations. Existing wireless sensing systems also commonly assume the target remains stationary during sensing. Resolving such challenges is crucial to make wireless sensing work in practical scenarios.

Severe dynamic interference. Based on our experiments with interference, we observe that RISensing is more robust against static non-target interference, such as leaping or standing still. However, when an interferer walks across the LoS path between the RIS and the target, or between the transmitter and the receiver, the sensing performance significantly degrades because the target is blocked. We leave this issue as a challenging yet interesting research direction for future work.

IX. CONCLUSION

In this paper, we present the design, implementation, and evaluation of RISensing, a system that deploys an RIS in the environment to enhance performance of Wi-Fi sensing. RISensing leverages RIS to generate a new target reflection signal, which can be carefully controlled to constructively combine with the original direct target reflection signal. We utilize the combination of two target reflection signals to address two fundamental issues in Wi-Fi sensing, i.e., limited sensing range and orientation-dependent issue. We conduct extensive experiments and demonstrate the effectiveness of RISensing in real-world setting. We believe the proposed RIS-based sensing model and signal processing methods can be applied to other RIS-based sensing modalities.

REFERENCES

[1] C. Wu, X. Huang, J. Huang, and G. Xing, "Enabling ubiquitous wifi sensing with beamforming reports," in *Proceedings of the ACM SIGCOMM 2023 Conference*, 2023, pp. 20–32.

[2] C. Feng, N. Wang, Y. Jiang, X. Zheng, K. Li, Z. Wang, and X. Chen, "Wi-learner: Towards one-shot learning for cross-domain wi-fi based gesture recognition," *Proceedings of the ACM on Interactive, Mobile, Wearable and Ubiquitous Technologies*, vol. 6, no. 3, pp. 1–27, 2022.

[3] B. Xie, J. Xiong, X. Chen, and D. Fang, "Exploring commodity rfid for contactless sub-millimeter vibration sensing," in *Proceedings of the 18th Conference on Embedded Networked Sensor Systems*, 2020, pp. 15–27.

[4] L. Li, Y. Xie, J. Xiong, Z. Hou, Y. Zhang, Q. We, F. Wang, D. Fang, and X. Chen, "Smartlens: Sensing eye activities using zero-power contact lens," in *Proceedings of the 28th Annual International Conference on Mobile Computing And Networking*, 2022, pp. 473–486.

[5] F. Zhang, Z. Chang, K. Niu, J. Xiong, B. Jin, Q. Lv, and D. Zhang, "Exploring lora for long-range through-wall sensing," *Proceedings of the ACM on Interactive, Mobile, Wearable and Ubiquitous Technologies*, vol. 4, no. 2, pp. 1–27, 2020.

[6] F. Zhang, Z. Chang, J. Xiong, R. Zheng, J. Ma, K. Niu, B. Jin, and D. Zhang, "Unlocking the beamforming potential of lora for long-range multi-target respiration sensing," *Proceedings of the ACM on Interactive, Mobile, Wearable and Ubiquitous Technologies*, vol. 5, no. 2, pp. 1–25, 2021.

[7] T. Wei and X. Zhang, "mtrack: High-precision passive tracking using millimeter wave radios," in *Proceedings of the 21st Annual International Conference on Mobile Computing and Networking*, 2015, pp. 117–129.

[8] B.-B. Zhang, D. Zhang, R. Song, B. Wang, Y. Hu, and Y. Chen, "Rf-search: Searching unconscious victim in smoke scenes with rf-enabled drone," in *Proceedings of the 29th Annual International Conference on Mobile Computing and Networking*, 2023, pp. 1–15.

[9] X. Song, B. Yang, G. Yang, R. Chen, E. Forno, W. Chen, and W. Gao, "Spirosonic: monitoring human lung function via acoustic sensing on commodity smartphones," in *Proceedings of the 26th Annual International Conference on Mobile Computing and Networking*, 2020, pp. 1–14.

[10] X. Fan, L. Shangguan, S. Rupavatharam, Y. Zhang, J. Xiong, Y. Ma, and R. Howard, "Headfi: bringing intelligence to all headphones," in *Proceedings of the 27th Annual International Conference on Mobile Computing and Networking*, 2021, pp. 147–159.

[11] Y. Wang, J. Liu, Y. Chen, M. Gruteser, J. Yang, and H. Liu, "E-eyes: device-free location-oriented activity identification using fine-grained wifi signatures," in *Proceedings of the 20th annual international conference on Mobile computing and networking*, 2014, pp. 617–628.

[12] H. Wang, D. Zhang, Y. Wang, J. Ma, Y. Wang, and S. Li, "Rt-fall: A real-time and contactless fall detection system with commodity wifi devices," *IEEE Transactions on Mobile Computing*, vol. 16, no. 2, pp. 511–526, 2016.

[13] J. Gong, X. Zhang, K. Lin, J. Ren, Y. Zhang, and W. Qiu, "Rf vital sign sensing under free body movement," *Proceedings of the ACM on Interactive, Mobile, Wearable and Ubiquitous Technologies*, vol. 5, no. 3, pp. 1–22, 2021.

[14] U. Ha, S. Madani, and F. Adib, "Wistress: Contactless stress monitoring using wireless signals," *Proceedings of the ACM on Interactive, Mobile, Wearable and Ubiquitous Technologies*, vol. 5, no. 3, pp. 1–37, 2021.

[15] Z. Chen, T. Zheng, C. Cai, and J. Luo, "Movi-fi: Motion-robust vital signs waveform recovery via deep interpreted rf sensing," in *Proceedings of the 27th annual international conference on mobile computing and networking*, 2021, pp. 392–405.

[16] Y. Zeng, J. Liu, J. Xiong, Z. Liu, D. Wu, and D. Zhang, "Exploring multiple antennas for long-range wifi sensing," *Proceedings of the ACM on Interactive, Mobile, Wearable and Ubiquitous Technologies*, vol. 5, no. 4, pp. 1–30, 2021.

[17] C. Feng, J. Xiong, L. Chang, J. Wang, X. Chen, D. Fang, and Z. Tang, "Wimi: Target material identification with commodity wi-fi devices," in *2019 IEEE 39th international conference on distributed computing systems (ICDCS)*.   IEEE, 2019, pp. 700–710.

[18] X. Wang, K. Niu, A. Yu, J. Xiong, Z. Yao, J. Wang, W. Li, and D. Zhang, "Wimeasure: Millimeter-level object size measurement with commodity wifi devices," *Proceedings of the ACM on Interactive, Mobile, Wearable and Ubiquitous Technologies*, vol. 7, no. 2, pp. 1–26, 2023.

[19] Y. Zeng, D. Wu, J. Xiong, E. Yi, R. Gao, and D. Zhang, "Farsense: Pushing the range limit of wifi-based respiration sensing with csi ratio of two antennas," *Proceedings of the ACM on Interactive, Mobile, Wearable and Ubiquitous Technologies*, vol. 3, no. 3, pp. 1–26, 2019.

[20] H. Wang, D. Zhang, J. Ma, Y. Wang, Y. Wang, D. Wu, T. Gu, and B. Xie, "Human respiration detection with commodity wifi devices: Do user location and body orientation matter?" in *Proceedings of the 2016 ACM international joint conference on pervasive and ubiquitous computing*, 2016, pp. 25–36.

[21] C. Feng, X. Li, Y. Zhang, X. Wang, L. Chang, F. Wang, X. Zhang, and X. Chen, "Rflens: metasurface-enabled beamforming for iot communication and sensing," in *Proceedings of the 27th Annual International Conference on Mobile Computing and Networking*, 2021, pp. 587–600.

[22] X. Li, C. Feng, X. Wang, Y. Zhang, Y. Xie, and X. Chen, "{RF-Bouncer}: A programmable dual-band metasurface for sub-6 wireless

networks," in *20th USENIX Symposium on Networked Systems Design and Implementation (NSDI 23)*, 2023, pp. 389–404.

[23] F. Marini and B. Walczak, "Particle swarm optimization (pso). a tutorial," *Chemometrics and Intelligent Laboratory Systems*, vol. 149, pp. 153–165, 2015.

[24] M. Li, Y. Meng, J. Liu, H. Zhu, X. Liang, Y. Liu, and N. Ruan, "When csi meets public wifi: inferring your mobile phone password via wifi signals," in *Proceedings of the 2016 ACM SIGSAC conference on computer and communications security*, 2016, pp. 1068–1079.

[25] K. Ali, A. X. Liu, W. Wang, and M. Shahzad, "Recognizing keystrokes using wifi devices," *IEEE Journal on Selected Areas in Communications*, vol. 35, no. 5, pp. 1175–1190, 2017.

[26] H. Li, W. Yang, J. Wang, Y. Xu, and L. Huang, "Wifinger: Talk to your smart devices with finger-grained gesture," in *Proceedings of the 2016 ACM International Joint Conference on Pervasive and Ubiquitous Computing*, 2016, pp. 250–261.

[27] L. Shangguan, Z. Zhou, and K. Jamieson, "Enabling gesture-based interactions with objects," in *Proceedings of the 15th Annual International Conference on Mobile Systems, Applications, and Services*, 2017, pp. 239–251.

[28] Y. Zheng, Y. Zhang, K. Qian, G. Zhang, Y. Liu, C. Wu, and Z. Yang, "Zero-effort cross-domain gesture recognition with wi-fi," in *Proceedings of the 17th annual international conference on mobile systems, applications, and services*, 2019, pp. 313–325.

[29] J. Zhang, Z. Tang, M. Li, D. Fang, P. Nurmi, and Z. Wang, "Crosssense: Towards cross-site and large-scale wifi sensing," in *Proceedings of the 24th annual international conference on mobile computing and networking*, 2018, pp. 305–320.

[30] J. Liu, Y. Wang, Y. Chen, J. Yang, X. Chen, and J. Cheng, "Tracking vital signs during sleep leveraging off-the-shelf wifi," in *Proceedings of the 16th ACM international symposium on mobile ad hoc networking and computing*, 2015, pp. 267–276.

[31] Y. Zeng, D. Wu, R. Gao, T. Gu, and D. Zhang, "Fullbreathe: Full human respiration detection exploiting complementarity of csi phase and amplitude of wifi signals," *Proceedings of the ACM on Interactive, Mobile, Wearable and Ubiquitous Technologies*, vol. 2, no. 3, pp. 1–19, 2018.

[32] Y. Li, D. Wu, J. Zhang, X. Xu, Y. Xie, T. Gu, and D. Zhang, "Diversense: Maximizing wi-fi sensing range leveraging signal diversity," *Proceedings of the ACM on Interactive, Mobile, Wearable and Ubiquitous Technologies*, vol. 6, no. 2, pp. 1–28, 2022.

[33] L. Chen, W. Hu, K. Jamieson, X. Chen, D. Fang, and J. Gummeson, "Pushing the physical limits of {IoT} devices with programmable metasurfaces," in *18th USENIX Symposium on Networked Systems Design and Implementation (NSDI 21)*, 2021, pp. 425–438.

[34] Z. Li, T. Jin, D. Guan, and H. Xu, "Metaphys: Contactless physiological sensing of multiple subjects using ris-based 4d radar," *IEEE Internet of Things Journal*, 2023.

[35] D. Xia, L. Guan, H. Liu, Y. Mu, X. Wang, J. Han, Y. Shi, and L. Li, "Metabreath: Multitarget respiration detection based on space-time-coding digital metasurface," *IEEE Transactions on Microwave Theory and Techniques*, 2023.

[36] X. Li, J. W. You, Z. Gu, Q. Ma, J. Zhang, L. Chen, and T. J. Cui, "Multiperson detection and vital-sign sensing empowered by space-time-coding reconfigurable intelligent surfaces," *IEEE Internet of Things Journal*, 2024.

[37] H. Zhang, J. Hu, H. Zhang, B. Di, K. Bian, Z. Han, and L. Song, "Metaradar: Indoor localization by reconfigurable metamaterials," *IEEE Transactions on Mobile Computing*, vol. 21, no. 8, pp. 2895–2908, 2020.

[38] Q. Luo, Z. Yang, B. Di, and C. Xu, "Meta2locate: Meta surface enabled indoor localization in dynamic environments," in *Proceedings of the Twenty-fourth International Symposium on Theory, Algorithmic Foundations, and Protocol Design for Mobile Networks and Mobile Computing*, 2023, pp. 312–313.

[39] D. Xie, X. Wang, and A. Tang, "Metasight: localizing blocked rfid objects by modulating nlos signals via metasurfaces," in *Proceedings of the 20th Annual International Conference on Mobile Systems, Applications and Services*, 2022, pp. 504–516.

[40] C. Li, Q. Huang, Y. Zhou, Y. Huang, Q. Hu, H. Chen, and Q. Zhang, "Riscan: Ris-aided multi-user indoor localization using cots wi-fi," in *Proceedings of the 21st ACM Conference on Embedded Networked Sensor Systems*, 2023, pp. 445–458.

[41] W. Wang, A. X. Liu, M. Shahzad, K. Ling, and S. Lu, "Understanding and modeling of wifi signal based human activity recognition," in *Proceedings of the 21st annual international conference on mobile computing and networking*, 2015, pp. 65–76.

[42] N. J. Willis, *Bistatic radar*.   SciTech Publishing, 2005, vol. 2.

[43] N. Jin and Y. Rahmat-Samii, "Advances in particle swarm optimization for antenna designs: Real-number, binary, single-objective and multiobjective implementations," *IEEE transactions on antennas and propagation*, vol. 55, no. 3, pp. 556–567, 2007.

[44] "Smp1340-040lf," https://www.skyworksinc.com/Products/Diodes/SMP1340-Series.

[45] D. Halperin, W. Hu, A. Sheth, and D. Wetherall, "Tool release: Gathering 802.11 n traces with channel state information," *ACM SIGCOMM computer communication review*, vol. 41, no. 1, pp. 53–53, 2011.

[46] R. K. Pearson, Y. Neuvo, J. Astola, and M. Gabbouj, "Generalized hampel filters," *EURASIP Journal on Advances in Signal Processing*, vol. 2016, pp. 1–18, 2016.

[47] Z. Wang, Z. Huang, C. Zhang, W. Dou, Y. Guo, and D. Chen, "Csi-based human sensing using model-based approaches: a survey," *Journal of Computational Design and Engineering*, vol. 8, no. 2, pp. 510–523, 2021.

[48] N. N. R. M. B. L. Sensor., "Nul-236," 2022, "https://www.amazon.com/NEULOG-Respiration-Monitor-Resolution-Maximum/dp/B00B76OZ9I".

[49] X. Wang, C. Yang, and S. Mao, "Phasebeat: Exploiting csi phase data for vital sign monitoring with commodity wifi devices," in *2017 IEEE 37th International Conference on Distributed Computing Systems (ICDCS)*. IEEE, 2017, pp. 1230–1239.

Xiaojing Wang received the B.E degree in Computer Science and Technology from Northwest University in 2020. She is currently working toward a Ph.D. degree in Software Engineering in the School of Information Science and Technology, Northwest University. Her research interests include ubiquitous computing, wireless sensing and mobile computing.

Binbin Xie received the Ph.D. degree from Manning College of Information and Computer Sciences, University of Massachusetts Amherst in 2024. She is currently a tenure-track assistant professor at Department of Computer Science and Engineering, University of Texas at Arlington. Her current research interests involve wireless sensing, mobile health, cyber-physical systems, and wireless networking.

Guanghui Lv received the B.E degree in Automation from Anhui Polytechnic University in 2022. He is currently working toward a M.S. degree in Software Engineering in the School of Information Science and Technology, Northwest University. His research interests include wireless sensing and mobile computing.

Boyang Liu received a B.E. degree in Communication Engineering from Xi'an University of Posts and Telecommunications in 2024. He is currently pursuing an M.S. degree in New Generation Electronic Information Technology at the School of Information Science and Technology, Northwest University. His research interests include wireless sensing and mobile computing.

Chenhao Ma received the B.E degree in Electronic Information Engineering from Xi'an University of Technology in 2023. He is currently working toward a M.S. degree in New Generation Electronic Information Technology in the School of Information Science and Technology, Northwest University. His research interests include wireless sensing and mobile computing.
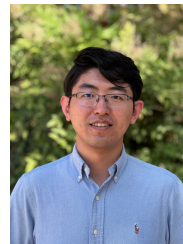
Renjie Zhao received the Ph.D. degree at Electrical and Computer Engineering Department in UC San Diego in 2023. He is currently an assistant professor in the Department of Computer Science at Johns Hopkins University. His current research interests include wireless networking and mobile computing.

Chao Feng received the Ph.D. degree in Computer Application Technology from Northwest University, Xi'an, China, in 2022. He is currently an associate professor at the school of Information Science and Technology, Northwest University, Xi'an. His current research interests include IoT localization, wireless sensing, and deep learning.

Xiaojiang Chen received the PhD degree in computer software and theory from Northwest University, Xi'an, China, in 2010. He is currently a professor at the School of Information Science and Technology, Northwest University. His current research interests include RF-based sensing and performance issues in internet of things.